Nanaerobic growth enables direct visualization of dynamic cellular processes in human gut symbionts

Leonor García-Bayona[a], Michael J. Coyne[a], Noam Hantman[b,c], Paula Montero-Llopis[d], Salena S. Von[a], Takeshi Ito[b], Michael H. Malamy[e], Marek Basler[f], Blanca Barquera[b,c], and Laurie E. Comstock[a,1]

[a]Division of Infectious Diseases, Brigham and Women's Hospital, Harvard Medical School, Boston, MA 02115; [b]Center for Biotechnology and Interdisciplinary Sciences, Rensselaer Polytechnic Institute, Troy, NY 12180; [c]Department of Biological Sciences, Rensselaer Polytechnic Institute, Troy, NY 12180; [d]MicRoN, Department of Microbiology, Harvard Medical School, Boston, MA 02115; [e]Department of Molecular Biology and Microbiology, Tufts University School of Medicine, Boston, MA 02111; and [f]Biozentrum, University of Basel, CH 4056 Basel, Switzerland

Edited by Lora V. Hooper, University of Texas Southwestern Medical Center, Dallas, TX, and approved August 12, 2020 (received for review May 13, 2020)

Mechanistic studies of anaerobic gut bacteria have been hindered by the lack of a fluorescent protein system to track and visualize proteins and dynamic cellular processes in actively growing bacteria. Although underappreciated, many gut "anaerobes" are able to respire using oxygen as the terminal electron acceptor. The oxygen continually released from gut epithelial cells creates an oxygen gradient from the mucus layer to the anaerobic lumen [L. Albenberg et al., Gastroenterology 147, 1055–1063.e8 (2014)], with oxygen available to bacteria growing at the mucus layer. Here, we show that *Bacteroides* species are metabolically and energetically robust and do not mount stress responses in the presence of 0.10 to 0.14% oxygen, defined as nanaerobic conditions [A. D. Baughn, M. H. Malamy, Nature 427, 441–444 (2004)]. Taking advantage of this metabolic capability, we show that nanaerobic growth provides sufficient oxygen for the maturation of oxygen-requiring fluorescent proteins in *Bacteroides* species. Type strains of four different *Bacteroides* species show bright GFP fluorescence when grown nanaerobically versus anaerobically. We compared four different red fluorescent proteins and found that mKate2 yields the highest red fluorescence intensity in our assay. We show that GFP-tagged proteins can be localized in nanaerobically growing bacteria. In addition, we used time-lapse fluorescence microscopy to image dynamic type VI secretion system processes in metabolically active *Bacteroides fragilis*. The ability to visualize fluorescently labeled *Bacteroides* and fluorescently linked proteins in actively growing nanaerobic gut symbionts ushers in an age of imaging analyses not previously possible in these bacteria.

fluorescent proteins | *Bacteroides* | nanaerobic | GFP | microbiota

The rapid increase in knowledge of the human gut microbiota and its impact on health and disease processes is the result of a multidisciplinary approach from microbiology, immunology, ecology, genomics, computational biology, and metabolomics, among others. The genetic toolkit to analyze bacterial members of this ecosystem has also greatly expanded in recent years (1–6), allowing better and faster analyses and mechanistic studies. Despite these advances, we have still been unable to use fluorescent proteins to visually track proteins or to visualize dynamic cellular processes in most gut symbionts due to the requirement of oxygen for the maturation of most fluorescent proteins.

The optimization of the flavin mononucleotide (FMN)-based fluorescent protein for use in anaerobic organisms brought hope for the development of a GFP equivalent for anaerobic microbes (7). Indeed, FMN-based fluorescent proteins have been successfully applied to studies of some anaerobes (8–10), but few studies have reported successful use of these or other fluorescent proteins in most anaerobic gut bacteria, especially in actively growing bacteria. Another approach to fluorescently label gut anaerobes used click chemistry to label surface polysaccharides (11). Bacteria metabolically labeled in vitro were tracked in vivo for up to 12 h before the fluorescent signal was lost from the surface. This labeling allowed imaging of polysaccharide association with immune cells (11). Recently, the bilirubin and biliverdin-binding proteins UnaG (green) and IFP2.0 (red) were shown to fluoresce in *Bacteroides* species grown under anaerobic conditions, allowing visualization of cytosolic and envelope-associated proteins in live cells, albeit requiring the addition of these ligands, laser excitation, and long exposure times during imaging (12).

Other fluorescent imaging techniques have been applied to study the spatial structure of bacterial communities. Advances in fluorescent in situ hybridization are illuminating the architecture of synthetic and natural microbial communities (13, 14), with the recent application of multiplexed fluorescence spectral imaging to image the spatial ecology of numerous different taxa of bacteria of the human tongue (15). A fluorescent protein-based analysis also revealed community structure in the mammalian gut (3). In this study, six different *Bacteroides* species were differentiated in vivo using constructs that resulted in three different levels of expression of GFP and mCherry by quantification of single-cell fluorescent profiles.

However, we still lack a bright fluorescent protein-based system to study live-cell processes in most gut anaerobes (reviewed in ref. 16). The human intestinal microbiota is dominated by bacteria that are considered to be strict anaerobes. Almost one-half of the gut bacteria in most healthy humans are members of the Gram-negative order Bacteroidales. These include numerous species of *Bacteroides*, *Parabacteroides*, *Prevotella*, *Alistipes*, and

Significance

Despite recent technological advances to study the human gut microbiota, we still lack a facile system to image dynamic cellular processes in most abundant gut species due to the requirement of oxygen for chromophore maturation of commonly used fluorescent proteins. Here, we took advantage of the ability of anaerobes of the gut microbiota to respire aerobically and grow robustly at 0.10 to 0.14% oxygen. This physiologic concentration of oxygen is sufficient for fluorescent proteins to mature, allowing for visualization of biological processes never before imaged in these bacteria. This advance will allow for numerous types of analyses in actively growing "nanaerobic" gut bacteria including subcellular protein localizations, single-cell analyses, biofilm imaging, and protein interactions with other microbes and the host.

Author contributions: L.G.-B., P.M.-L., M.H.M., M.B., B.B., and L.E.C. designed research; L.G.-B., N.H., S.S.V., T.I., B.B., and L.E.C. performed research; L.G.-B., M.J.C., P.M.-L., M.B., B.B., and L.E.C. analyzed data; and L.G.-B., M.J.C., and L.E.C. wrote the paper.

The authors declare no competing interest.

This article is a PNAS Direct Submission.

[1]To whom correspondence may be addressed. Email: lcomstock@rics.bwh.harvard.edu.

This article contains supporting information online at https://www.pnas.org/lookup/suppl/doi:10.1073/pnas.2009556117/-/DCSupplemental.

First published September 16, 2020.

others. The gut microbiota also contains a large proportion of members of the phylum Firmicutes, which includes many diverse families. Some, such as the members of the *Clostridiaceae* family, are strict anaerobes, while others, such as members of the *Lactobacillaceae* family, have varying abilities to grow in room air. In addition, there are abundant genera of other phyla including Actinobacteria and Verrucomicrobia with varying abilities to grow in the presence of oxygen.

Cytochrome *bd* is one of the terminal oxidases of aerobic respiration in prokaryotes (reviewed in ref. 17). In contrast to many heme-copper oxidases that are typically expressed when bacteria are grown in high aeration, cytochrome *bd* is usually expressed in low oxygen conditions. This likely reflects the fact that cytochrome *bd* has a much higher affinity for oxygen than most heme-copper oxidases (18, 19). Cytochrome *bd* accepts electrons from quinols and donates them to oxygen to make water. The enzyme generates an electrochemical proton gradient by a membrane charge separation. In this way, cytochrome *bd* is able to conserve the energy from nanaerobic respiration for use by the cell (20).

Among the abundant gut symbionts, *Bacteroides* species and *Akkermansia mucinophila* have been shown to have cytochrome *bd* and to respire using oxygen as the terminal electron acceptor (21, 22). This metabolic capability was shown in both *Bacteroides fragilis* and *A. mucinophila* to lead to the consumption of oxygen during nanaerobic growth. In this study, we show that the nanaerobic oxygen concentration under which *Bacteroides* species likely grow and thrive when at the mucus layer is sufficient to allow for the maturation of commonly used fluorescent proteins in order to image active processes in healthy, metabolically active bacterial cells.

Results

Analysis of *B. fragilis* Grown under Nanaerobic Conditions. Four commonly studied *Bacteroides* strains, *B. thetaiotaomicron* VPI-5482, *B. ovatus* ATCC 8483, *B. vulgatus* ATCC 8482, and *B. fragilis* 638R, all grow robustly in a nanaerobic atmosphere (0.1 to 0.14% or 1,000 to 1,400 ppm atmospheric oxygen) as previously shown (21), reaching a maximal OD_{600} similar to that reached during anaerobic growth (Fig. 1*A* and *SI Appendix*, Fig. S1). During anaerobic respiration in *Bacteroides*, fumarate reductase is the terminal component of the pathway, transferring electrons from quinols to fumarate. To show a benefit from nanaerobic growth, we made a *B. fragilis* mutant deleted for the three fumarate reductase genes *frdABC*. The Δ*frd* mutant is severely defective for growth under anaerobic conditions, but its growth is improved under nanaerobic conditions (Fig. 1*A* and ref. 21).

To determine potential differences in the physiology of *Bacteroides* when cultured with or without nanaerobic concentrations of oxygen, we performed RNA-seq analysis of *B. fragilis* 638R. Using a strict cutoff for differential expression of at least 1.5-fold and an adjusted *P* value less than or equal to 0.001, of the total 4,332 genes, there were 171 genes up-regulated and 405 genes down-regulated under nanaerobic growth compared to anaerobic growth (Fig. 1*B* and Dataset S1). Most categories of genes based on clusters of orthologous groups of proteins (COG) assignment were split between being more highly expressed under anaerobic or nanaerobic conditions (*SI Appendix*, Fig. S2). For example, 13 *susCD* genes involved in the transport of carbohydrates and other nutrients across the outer membrane are up-regulated under nanaerobic conditions. Under anaerobic conditions, 17 distinct *susCD* genes are more highly expressed. In terms of transcriptional regulators, 18 genes of at least six different families are more highly expressed under anaerobic conditions and six are more highly expressed under nanaerobic conditions (Dataset S1).

We next analyzed the RNA-seq data to determine whether the bacteria mount an oxidative stress response when grown nanaerobically. A prior study identified the *B. fragilis* transcriptional responses when exposed to room oxygen, 5% oxygen, or H_2O_2 (23). In that study, 30 genes classified as involved in stress responses were highly up-regulated under at least one of the three stress conditions. Of these 30 genes, only three were significantly up-regulated during nanaerobic growth, and 13 were significantly down-regulated (Table 1). Genes encoding catalase and superoxide dismutase, two enzymes that are involved reactive oxygen species response, were not differentially expressed between the two conditions.

Our analysis showed that of the 4,241 protein-encoding genes of strain 638R, 3,030 genes are core genes of *B. fragilis*. Four hundred of these core genes are differentially expressed; 142 (4.7%) are up-regulated and 258 (8.5%) are down-regulated under nanaerobic conditions (Fig. 1*B* and Dataset S1). In total, 2,630 of the core genes (86.8%) were not differentially expressed. Of the 550 previously identified essential genes of *B. fragilis* 638R (24) (494 of which were retained in the RefSeq genome annotation NC_016776.1), 372 are also core genes of *B. fragilis* (Dataset S1). Here, we show that of those core essential genes, only 12 were significantly differentially regulated between the two conditions (Fig. 1*B*). Three are more highly expressed under nanaerobic conditions, and nine are more highly expressed under anaerobic conditions (Fig. 1*B*).

Next, we sought to determine whether a cellular process that requires large amounts of ATP is as active in bacteria grown nanaerobically. The type VI secretion system is a dynamic intercellular antagonistic system that requires the assembly and disassembly of a toxin-loaded tube enclosed within a contractile sheath. After contraction of the sheath with subsequent propulsion of the tube across both membranes, the sheath is disassembled by ClpV (TssH). ClpV is an AAA+ ATPase (25) that uses the energy from ATP hydrolysis to mechanically disassemble the sheath structure (26). We found that *B. fragilis* 638R cocultured under nanaerobic conditions with sensitive strain *B. vulgatus* CL09T03C04 shows similar T6SS killing activity as when cultured under anaerobic conditions (2-log reduction of target strain under both conditions; Fig. 1*C*). The RNA-seq data revealed that nearly all genes of this T6SS locus are up-regulated under nanaerobic conditions; however, only two of these genes reached significance by the criteria used in this study (Dataset S1). These data suggest that the GA3 T6SS of *B. fragilis* is functionally relevant at the oxygenated mucus layer as previously predicted (27, 28). These data collectively demonstrate that although there are transcriptional differences between anaerobic and nanaerobic growth, nanaerobically grown bacteria have similar transcriptional profiles of the vast majority of essential core genes as their anaerobically grown counterparts, are not undergoing general stress responses, and are metabolically and energetically active.

Prevalence of Cytochrome *bd* Genes in the Bacteroidales. Bacteroidales is an order of bacteria that contains not only gut species of the genera *Bacteroides*, *Parabacteroides*, *Prevotella*, and *Alistipes*, but also oral pathogens such as *Porphyromonas gingivalis*, *Tannerella forsythia*, oral *Prevotella* species, as well as vaginal species and species that occupy other mammalian ecosystems. Cytochrome *bd* encoding genes, *cydAB*, were shown to be present in numerous *Bacteroides* species as well as *P. gingivalis* and *Prevotella intermedia* (21). In addition, a 2013 study using tBLASTx identified *cydAB* in 51 Bacteroidetes genomes (29); however, the species identifications within this large phylum were not provided. To determine the potential for nanaerobic growth of other species of Bacteroidales, nearly all of which associate with mammalian hosts, we queried a representative strain of 173 different species, contained within 32 genera and 13 families of Bacteroidales for pfams PF01654.17 and PF02322.15 specific to CydA and CydB, respectively. Protein sequences matching these models were detected in the genomes of 163

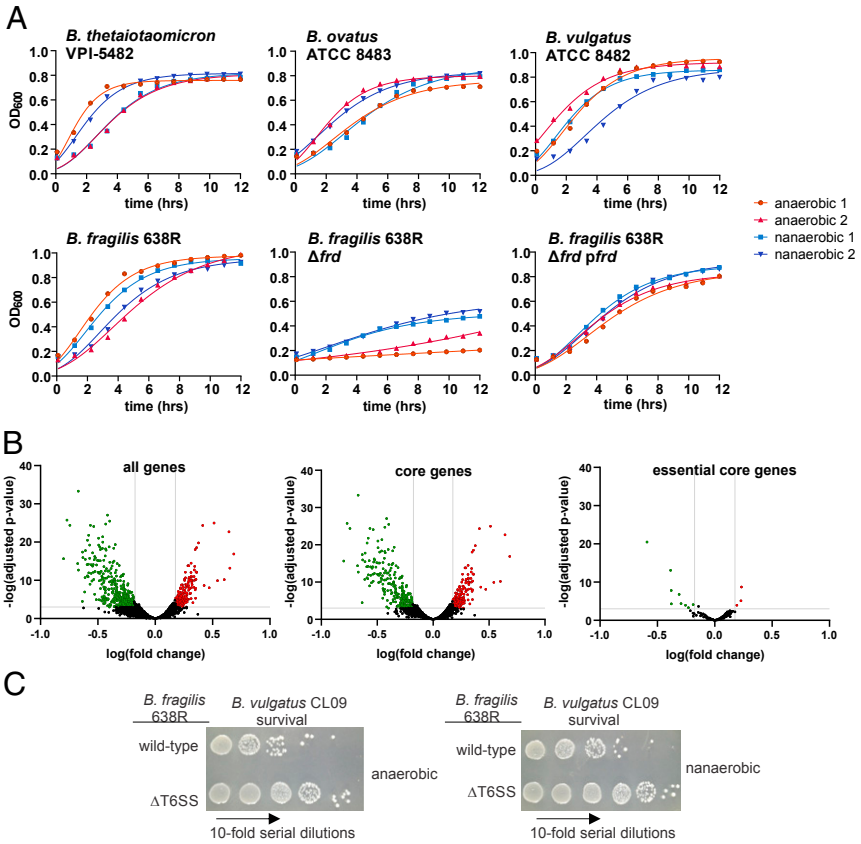

Fig. 1. Analysis of nanaerobic growth properties of *Bacteroides*. (*A*) Growth curves of four *Bacteroides* species and the *B. fragilis* Δ*frd* mutant and complemented mutant Δ*frd* p*frd* under anaerobic and nanaerobic conditions. (*B*) Volcano plot showing differential expression of the 4,332 genes of *B. fragilis* 638R (*Left*), the 3,030 core genes of *B. fragilis* (*Middle*), and the 372 core essential genes of *B. fragilis* 638R (*Right*) under nanaerobic compared to anaerobic growth. The green dots represent genes significantly down-regulated under nanaerobic conditions, and red dots represent up-regulated genes (significance defined as at least 1.5-fold and adjusted *P* value (DESeq2) and FDR (edgeR) both were less than or equal to 0.001. (*C*) Analysis of the ability of the *B. fragilis* GA3 T6SS to antagonize sensitive strain *B. vulgatus* CL09T03C04 under both anaerobic and nanaerobic conditions.

species (Dataset S2). Of the remaining 10 genomes, 5 contained *cydB*, 3 of which also had a *cydA* gene containing one or more frameshifts. These data suggest that species of the order Bacteroidales that occupy diverse host ecosystems have the ability to respire aerobically under low oxygen conditions, transferring electrons from reduced quinone to oxygen via cytochrome *bd*, and will likely grow under nanaerobic conditions.

Analysis of Fluorescence of Green and Red Fluorescent Proteins from Nanaerobically Grown *Bacteroides* Species. We sought to take advantage of this normal physiological property of these bacteria to determine whether 0.10 to 0.14% oxygen is sufficient to mature GFP for imaging analyses. We used a plasmid created in the laboratory of J. L. Sonnenburg, Stanford University School of Medicine, Stanford, CA, pWW3452, which contains an optimized promoter sequence and ribosome binding site resulting in very high GFP levels in *Bacteroides* (3) using the superfolder GFP gene (referred to as GFP throughout the paper) (30). This construct was created in the pNBU2-erm backbone vector that integrates into *Bacteroides* chromosomes (31). *Bacteroides* species containing pWW3452 were shown to fluoresce when grown anaerobically with subsequent exposure to oxygen for 60 min (3). We transferred pWW3452 into the chromosomes of four *Bacteroides* species and grew them under strict anaerobic conditions or in an atmosphere of 0.10 to 0.14% oxygen (1,000 to 1,400 ppm). After 4 h of growth with shaking, cultures were added to agarose pads on microscope slides and sealed in their respective atmospheres in the chambers. Microscopic analysis revealed bright green fluorescence from bacteria grown nanaerobically but not anaerobically (Fig. 2 *A* and *B*). A similar analysis of the mCherry equivalent plasmid, pWW3515, revealed weak mCherry fluorescence when *B. fragilis* 638R was grown nanaerobically (Fig. 2*C*). We attempted to improve the red fluorescence by analyzing three additional red fluorescent proteins, DsRed2, mKate2, and TagRFP. We replaced the GFP gene of pWW3452 with codon-optimized genes encoding each of these proteins (*SI Appendix*, Fig. S3) and transferred the resulting plasmids into *B. fragilis*. Frequency distribution analysis of the images revealed that mKate2 produced the brightest fluorescence of the four red proteins (Fig. 2 *C* and *D* and *SI Appendix*, Fig. S4). Therefore, the chromophores of GFP and mKate2 (along with mCherry and TagRFP to a lesser extent) mature to a significant level under nanaerobic conditions so that *Bacteroides* harboring them can be fluorescently imaged.

GFP Labeling of Proteins to Track Subcellular Localization. To test whether we could use this process to label and track proteins in actively growing *Bacteroides*, we linked GFP to genes encoding two proteins secreted in outer membrane vesicles (OMVs). BACOVA_04502 of *B. ovatus* ATCC 8483 encodes an inulin lyase (32–34) and was previously shown to be secreted in OMVs by concentration of OMVs by two rounds of ultracentrifugation of culture supernatants followed by activity assays (33). To determine whether we could visualize this protein in OMVs, we

Table 1. Comparison of differentially expressed genes under oxidative stress as previously reported (23) versus nanaerobic growth

9343*	638R†	Gene	Function and COG class‡	Fold induction§			FC¶	*P* adj#
				H_2O_2	Air	5% O_2	Nanoaerobic	
Detoxification								
BF1195	BF638R_1262	*katB*	Catalase (P)	28	46	53	−1.6	4.49E-03
BF1209	BF638R_1275	*ahpF*	Alkyl hydroperoxide reductase subunit (O)	70	32	86	−2.2	7.51E-12
BF1210	BF638R_1276	*ahpC*	Alkyl hydroperoxide reductase subunit (O)	77	76	93	−1.0	9.86E-01
BF2360	BF638R_2372	*Tpx*	Thioredoxin peroxidase (O)	7	12	10	1.8	8.22E-07
BF2556	BF638R_2545	*Sod*	Superoxide dismutase (P)	—	8	4	−1.2	4.54E-01
BF2777	BF638R_2786	*Tps*	Thiol peroxidase-scavengase (O)	—	6	—	−1.5	2.38E-02
BF3656	BF638R_3727	*Glp*	Glutathione peroxidase (O)	—	14	—	−1.4	3.75E-02
BF2268	BF638R_2327	*Dyp*	Dyp-type peroxidase (P)	—	5	5	−1.7	1.78E-04
BF2362	BF638R_2374	*ccp1*	Cytochrome-C peroxidase (P)	3	—	—	3.3	7.06E-28
Metal metabolism								
BF1317	BF638R_1333	*Dps*	DNA and iron binding (P)	25	38	45	−3.4	6.02E-17
BF2884	BF638R_2891	*ftnA*	FerritinA, nonhaem iron (P)	—	4	—	1.0	9.66E-01
BF3271	BF638R_3305	*Bfr*	Bacterioferritin (R)	—	22	—	−5.5	4.08E-25
BF3032	BF638R_3039	*pir2*	Pirin (R) iron, cupin family	—	15	6	−2.3	2.13E-15
BF3190	BF638R_3217	*nlpE*	Copper resistance; signaling for Cpx pathway (P)	—	9	—	1.7	5.47E-06
Nucleic acid repair								
BF1191	BF638R_1258	*Nfo*	Endonuclease IV (L)	—	4	—	−1.1	3.12E-01
BF1780	BF638R_4381	*radC*	RecG-like activity (L)	—	—	3	−2.2	4.20E-04
BF1945	BF638R_1917	*mgs1*	AAA-family ATPase, Holliday junction repair (L)	—	4	—	−1.1	4.16E-01
BF2642	BF638R_2636	*uvrB*	UvrB SOS-repair system (L)	—	—	3	1.2	2.30E-02
BF3312	BF638R_3340	*Ung*	Uracil-DNA glycosylase (L)	—	6	—	−2.7	6.00E-19
BF4111	BF638R_4168	*Ada*	Methylated-DNA – protein-cysteine methyltrans (L)	—	3	—	1.3	6.71E-03
Protein repair/chaperones								
BF1172	BF638R_1237	*clpA*	Chaperone ATPase (O)	—	12	—	−2.2	6.11E-08
BF3207	BF638R_3234	*dnaJ*	DnaJ; chaperone for protein aggregates (O)	—	10	—	−2.2	1.07E-12
BF3378	BF638R_3405	*msrA*	Methionine sulfoxide reductase (O)	—	12	11	−1.3	6.08E-03
Redox balance								
BF1279	BF638R_1294	*trxG*	Thioredoxin (O)	—	14	—	−2.8	5.54E-09
BF2237	BF638R_2295	*trxD*	Thioredoxin (O)	3	8	13	1.1	3.69E-01
BF2656	None	*trxX*	Thioredoxin-like no conserved cysteines (O)	—	5	—		
BF2694	BF638R_2701	*trxC*	Thioredoxin-exported (O)	—	7	—	1.2	4.47E-01
BF3015	BF638R_3022	*trxEF*	Thioredoxin (O)	—	7	6	−1.7	1.23E-04
General function								
BF2495	BF638R_2455	*uspA*	Universal stress protein (T)	—	16	5	−1.8	2.77E-04
BF2778	BF638R_2787	*Oim*	Membrane protein; HdeD domain, acid defense (S)	—	9	—	−2.7	4.51E-08

B. fragilis NCTC 9343 stress response genes up-regulated during exposure to H_2O_2, air, or 5% oxygen. Reproduced with permission from ref. 23.
*Original *B. fragilis* NCTC 9343 locus tags.
†Cross-genome gene equivalency was determined by reciprocal best-hit analysis using BLASTp. Locus tag names for *B. fragilis* 638R from RefSeq accession no. NC_016776.1.
‡COG classes: L, replication, recombination, and repair; O, protein fate and chaperones; P, inorganic ion metabolism and transport; R, general function; S, no functional prediction; and T, signal transduction as reported (54).
§Fold induction as determined by ANOVA analysis of the Nimblegen microarray expression data. Only genes considered to be overexpressed relative to anaerobic conditions are enumerated (see ref. 23).
¶,#Fold change (FC)¶ and adjusted *P* values (*P* adj)# as calculated by DESeq2 (51). Highlighted entries indicate significant ($P < 0.001$) differential expression of greater than 1.5-fold differential expression; red/green highlighting denotes overexpression or underexpression compared to anaerobic conditions, respectively.

created a linker-GFP construct by altering pWW3452 (Fig. 3 *A*, *C*, and *D*), fused the inulinase gene in frame, and transferred it to *B. ovatus*. Fluorescence microscopic analysis showed that the protein was present in the membrane and showed bright fluorescence in OMVs. Moreover, we could visualize inulinase-loaded OMVs vesiculating from the cell surface (Fig. 3*D*). This is in stark contrast to the cytoplasmic localization of unlinked GFP (Figs. 2*B* and 3*B*), and the lack of labeling of OMVs in these strains.

Similarly, we cloned into pLinkerGFP the BSAP-1 gene (BF638R_1646) of *B. fragilis*, encoding a MACPF domain antimicrobial toxin (35). BSAP-1 was previously shown to be secreted in OMVs by ultracentrifuging OMVs from culture supernatant and then performing immunofluorescence labeling using a primary antibody specific to BSAP-1 and a FITC-labeled secondary antibody (35). Here, we integrated the *bsap1-linker-gfp* fusion plasmid into the chromosome of the *bsap*-1 mutant strain. We first confirmed that the toxin was active with the C-terminal GFP fusion. The agar overlay shows that BSAP-1-GFP is able to restore antibacterial toxin activity to the *bsap-1* deletion mutant (Fig. 3*E*). Using fluorescence microscopic analysis of the BSAP1-GFP fusion, we observed it in the membrane of the bacteria and also in OMVs (Fig. 3*G*). As with the *B. ovatus* inulinase, instances of BSAP-1 in OMVs vesiculating from the cell were frequently observed. Similarly, fluorescence is absent in OMVs and membranes of the *B. fragilis* strain expressing the unlinked

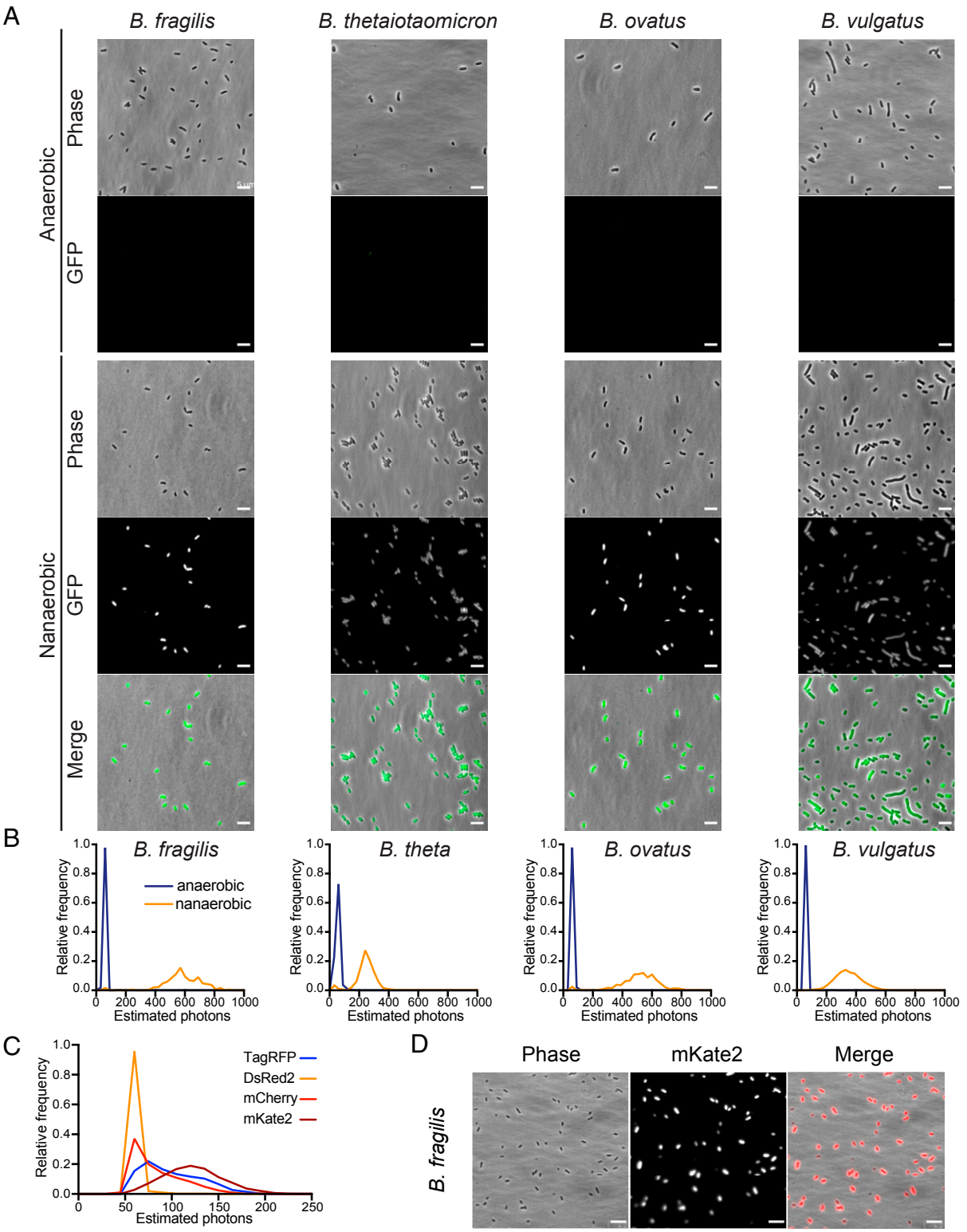

Fig. 2. Nanaerobic growth allows fluorescent imaging of *Bacteroides* species. (*A*) Epifluorescent microscopy of indicated *Bacteroides* species expressing GFP, grown under aerobic and nanaerobic conditions. (Scale bars, 5 μm.) (*B*) Frequency distribution of single-cell mean green signal intensity in cells of the indicated species expressing GFP. (*C*) Frequency distribution of red fluorescence signal intensity in *B. fragilis* cells expressing the indicated red fluorescent protein grown under nanaerobic conditions. (*D*) Epifluorescent microscopy of *Bacteroides fragilis* expressing mKate2, grown under nanaerobic conditions. (Scale bars, 5 μm.)

cytosolic GFP (Fig. 3*F*). In sum, this process allows visualization and localization of two cytosolic proteins (unlinked GFP and mKate) and two OMV-associated proteins in live bacteria without the need to generate a specific antibody, perform an activity assay, or poison the cells by atmospheric oxygen exposure.

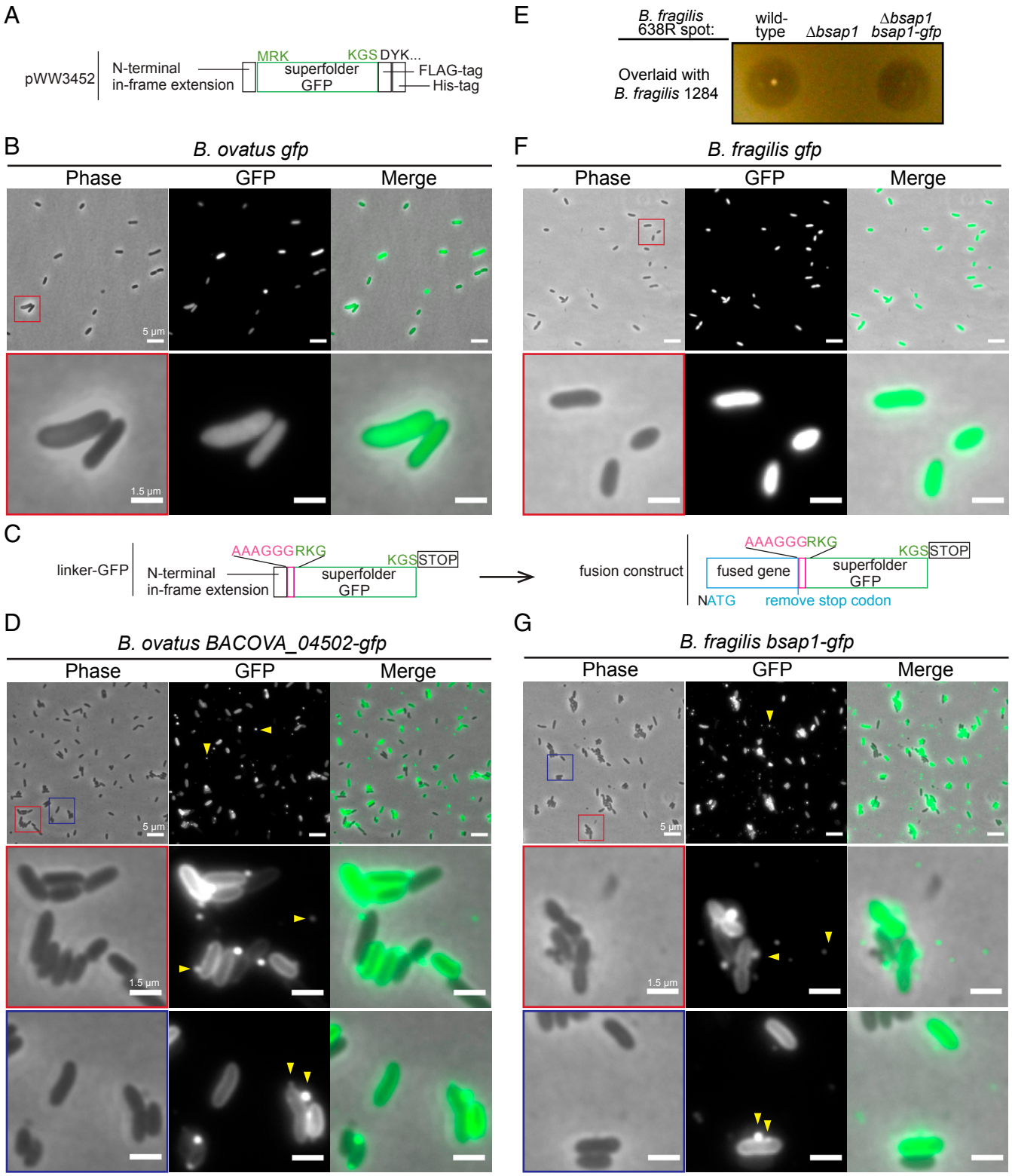

Fig. 3. Localization of GFP-linked proteins in *B. fragilis*. (*A*) Diagram of the superfolder GFP expression cassette of plasmid pWW3452 (3). (*B* and *F*) *Bacteroides ovatus* and *B. fragilis* with pWW3452 display cytosolic localization of GFP. Second row corresponds to magnified field (scale bars, 1.5 μm) of the area indicated in red in the top row (scale bars, 5 μm). (*C*) Modifications made to pWW3452 to create pLinkerGFP (*Left* construct) and the addition of upstream genes to create fusion proteins with linker-GFP (*Right*). N represents an additional nucleotide introduced to shift reading frame relative to N-terminal in-frame extension. (*D*) *B. ovatus* expressing GFP-fused BACOVA_04502, encoding an inulinase, which is secreted in outer membrane vesicles (OMVs) (indicated with yellow arrows). Second and third rows correspond to magnified images (scale bars, 1.5 μm) of the areas indicated in red and blue in the top row (scale bars, 5 μm). (*E*) Agar overlay assay of BSAP-1 sensitive strain *B. fragilis* 1284 to growth inhibition by the indicated *B. fragilis* 638R strains. (*G*) *B. fragilis* expressing GFP-fused BSAP-1, which is abundantly secreted in OMVs (indicated with yellow arrows). Second and third rows correspond to magnified images (scale bars, 1.5 μm) of the areas indicated in red and blue in the top row (scale bars, 5 μm).

Time-Lapse Microscopy Reveals Dynamic Type VI Secretion System Processes in *B. fragilis*. Time-lapse microscopy of fluorescently labeled T6SS structural components has played a key role in understanding the dynamics, regulation, and mechanics of T6SS firing in many Proteobacterial species (reviewed in ref. 36). *Bacteroides* species harbor three different architectures of T6SS, termed GA1–3 (37), which are largely still unexplored. *B. fragilis* 638R harbors a GA3 T6SS, which has been shown to kill *Bacteroides* species under anaerobic (27, 38, 39) and, in this study, under nanaerobic conditions (Fig. 1*C*). We made a deletion mutant of BF638R_1993, encoding the GA3 T6SS protein TssB, one of two sheath proteins. In Proteobacterial species growing in air, this protein has been successfully fused to GFP to visualize sheath extension and contraction (40). We cloned the *B. fragilis* 638R *tssB* into pLinkerGFP to synthesize a TssB-GFP fusion and introduced it into *B. fragilis* 638R Δ*tssB*. To confirm that the fusion to GFP did not abrogate TssB function, we tested whether the T6SS was still able to function using two different assays. First, we assayed for the presence of the tube protein, TssD, in the culture supernatant. There is no TssD tube protein in the supernatant of the Δ*tssB* mutant, and addition of the p*tssB-gfp* construct to the Δ*tssB* mutant restored TssD secretion (Fig. 4*A*). In the second assay, we used antagonism of sensitive strain *B. vulgatus* CL09T03C04 as a readout for T6SS function. The complemented mutant restored the 2-log killing to the Δ*tssB* mutant, comparable to the level of antagonism by wild type (Fig. 4*B*). Therefore, as was demonstrated with the GFP fusion to the TssB protein in Proteobacterial species, this fusion does not interfere with the function of TssB.

Next, we analyzed whether we could use the Δ*tssB*::p*tssB-gfp* strain to perform live-cell time-lapse imaging of T6SS sheath assembly and contraction. Bacteria were grown nanaerobically for 5 h, spotted on an agarose pad, sealed nanaerobically in a glass-bottom dish, and imaged at 37 °C. In the majority of cells, TssB displayed diffuse cytosolic fluorescence and mobile foci, indicative of a contracted sheath or aggregates (Fig. 4*C* and *SI Appendix*, Fig. S5). Many cells had one or more extended sheaths, which did not appear to have a preferred orientation relative to the axis of the cell (Fig. 4*C*, *SI Appendix*, Fig. S5, and Movies S1 and S2). Sheath contraction was very rapid, going from a fully extended to fully contracted sheath between single frames, indicating contraction in less than 10 s. The contracted sheath was approximately one-half the length of the extended sheath.

Visualization of the contraction–disassembly cycle (Fig. 4*C* and Movies S1 and S2) indicates that multiple sheaths can be present in the same cell. Under the conditions in which these bacteria were imaged, sheath assembly was very rarely observed, even though cells with extended sheaths were abundant. The sheaths often remained extended for several minutes before contracting. The timing of disassembly of contracted sheaths was highly variable between cells and often lasted longer than 50 s. After firing, many of the TssB-GFP fluorescent foci moved within the cell during disassembly.

The ability to image nanaerobic bacteria for extended periods of time and to image dynamic processes that occur over the cell cycle requires that the cells stay viable and divide under the conditions of our assay. To ensure that the imaging method described in this study allows for such imaging and that toxic levels of oxygen are not introduced into the system over time, we used time lapse-microscopy. Movie S3 shows both bacterial growth and division on the agar pads under the conditions of our assay, allowing for the imaging of numerous active processes in dividing nanaerobic bacteria.

Analysis of Presence of Cytochrome *bd* in Other Sequenced Human Gut Bacteria. To determine whether other gut bacteria currently known to grow only under anaerobic conditions may also be able to grow under nanaerobic conditions and therefore may be amenable to fluorescent protein imagining analyses, we searched for protein sequences matching the same CydAB profile Hidden Markov models used to query the Bacteroidales genome set. For this analysis, 612 genomes of the Human Gastrointestinal Bacteria Culture Collection (41) that contained protein translations and that were retrievable as assembled genomes from the National Center for Biotechnology Information (NCBI) databases were queried (Dataset S3). As shown above, the gut Bacteroidales uniformly contain cytochrome *bd*. There was variability in the phylum Actinobacteria, with some genera containing CydAB and others, such as *Bifidobacterium*, lacking them. *Eggerthella lenta* and several other species in the Eggerthellaceae family contain CydAB. Members of this species have been shown to inactivate the cardiac drug digioxin (42). Among the Firmicutes, many members of the class Bacilli are known to grow in the presence of oxygen, including many *Lactobacilli*, and most species in this class have CydAB. However, those in the class Clostridiales are strict anaerobes and lack CydAB. Among less studied Firmicutes, several genera in the class Negativicutes contain CydAB, including *Veillonella*, *Megamonas*, and *Mitsuokella*. Therefore, in addition to the Bacteroidales and *Akkermansia*, there are potentially other gut bacteria currently classified as strict anaerobes that may be amenable to nanaerobic growth and the use of fluorescent protein analysis if gene transfer systems are available and if nanaerobic growth does not induce a damaging oxidative stress response.

Discussion

The most important aspect of this study to the gut microbiome field is the application of nanaerobic growth to fluorescently image proteins and dynamic cellular processes in actively growing "nanaerobic" gut symbionts. In this regard, it was important to establish that growth under nanaerobic conditions is a normal process of these bacteria. Since the identification of nanaerobic respiration in *Bacteroides* in 2004 (21), there have been no further analyses of this process, and therefore, our understanding was very limited. Transcriptomic analysis of these two conditions has been very illuminating. Very few core essential genes are differentially expressed under the two conditions and there is no evidence of a general stress response during nanaerobic growth. In fact, many of the genes previously identified as up-regulated during stress response to H_2O_2 or high levels of oxygen are more highly expressed under anaerobic conditions. A transcriptomic analysis of the anaerobic sulfate-reducing bacterium *Desulfovibrio vulgaris* showed a similar lack of up-regulation of most of the oxidative stress response genes during growth at 0.1% oxygen compared to exposure to air (43). Oxygen is continually released from intestinal epithelial cells, creating an oxygen gradient that rapidly decreases from the mucus layer to the anaerobic lumen (44). As *Bacteroides* are present at both the mucus layer and in the lumen, it is not surprising that these bacteria have different transcriptional programs based on whether they find themselves in the presence or absence of nanaerobic concentrations of oxygen. It will be interesting to determine the functions of various gene products that are differentially regulated under each condition including the various transcriptional regulators, SusCD outer membrane nutrient transporters, and fimbriae genes, 11 of which are more highly expressed under anaerobic conditions.

There are numerous applications for the use of nanaerobic growth to fluorescently image these bacteria and their proteins, allowing for types of analyses not easily performed using other methodologies. Such studies include the tracking of protein subcellular localizations and secretion. Here, we show that we can readily localize proteins to OMVs, which have been shown in numerous studies to be loaded with molecules essential for interactions with other bacteria and the host (33, 35, 45–49). Furthermore, as the chromophores of both red and green

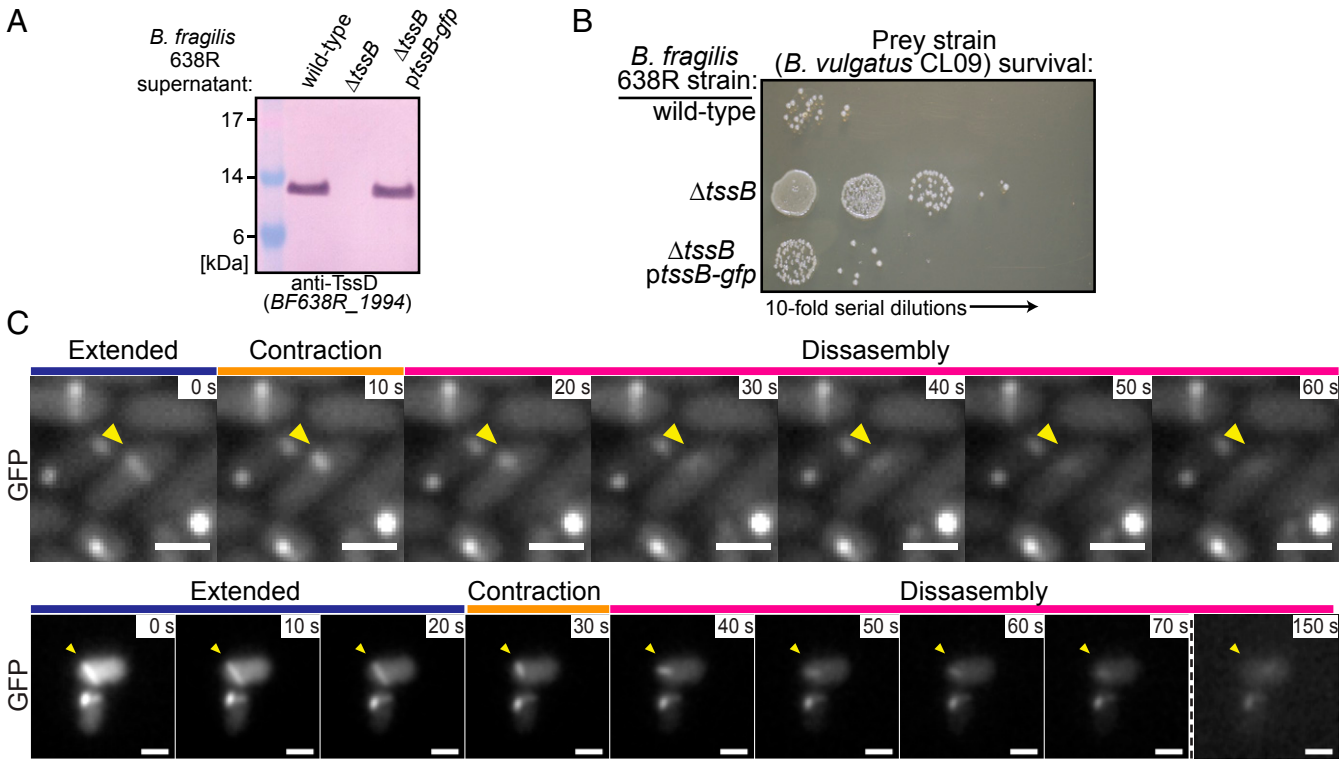

Fig. 4. Fluorescence imaging of T6SS sheath dynamics in *B. fragilis*. (*A*) Western immunoblot of culture supernatants from the indicated *B. fragilis* strains, probed with antiserum to TssD. (*B*) T6SS antagonism assays with *B. fragilis* strains against the sensitive strain *B. vulgatus* CL09T03C04. Strains were cocultured overnight under anaerobic or nanaerobic conditions, and survival of the sensitive strain was quantified by serial 10-fold dilutions on selective media. (*C*) Time-lapse of two representative Δ*tssB::ptssB-gfp* cells undergoing T6SS firing (yellow arrows). (Scale bars, 1 μm.)

proteins mature under nanaerobic conditions, protein–protein interactions and colocalization studies in metabolically active bacteria are possible. Additionally, numerous types of single-cell analyses are possible to study transcriptional and phenotypic heterogeneity among a population of bacteria. Also, this process should allow for imaging of biofilm and multispecies structures in flow cells. The real-time imaging of *B. fragilis* GA3 T6SS sheath assembly and contraction demonstrates the ability to image dynamic cellular processes in these gut bacteria. In summary, for nanaerobic bacteria such as the *Bacteroides*, fluorescent protein imaging is now an available tool to explore numerous aspects of bacterial cell biology.

Methods

Growth of Bacterial Strains. *Bacteroides* wild-type strains used in the study include *B. fragilis* 638R, *B. thetaiotaomicron* VPI-5482, *B. ovatus* ATCC 8483, and *B. vulgatus* ATCC 8482. *Bacteroides* strains were grown in BHI broth supplemented with 5 g/L yeast extract and 5 μg/mL hemin (BHIS broth). Where appropriate, antibiotics were added: carbenicillin, 100 μg/mL; erythromycin, 5 μg/mL; gentamycin, 200 μg/mL; tetracycline, 6 μg/mL. *Bacteroides* were grown on BHIS plates, which is BHI supplemented with 5 μg/mL hemin and 2.5 μg/mL vitamin K1. In some cases, modified M9 medium was used, which is M9 minimal medium with 0.5% (wt/vol) glucose, cysteine to 0.025%, 5 μg/mL hemin, 2.5 μg/mL vitamin K1, 2 μg/mL $FeSO_4$ $7H_2O$, and 5 ng/mL vitamin B_{12}. For nanaerobic growth, oxygen and hydrogen levels were continually monitored using a CAM-12 gas monitor (Coy Lab Products).

Creation of Fumarate Reductase (*frd*) Mutation and Complementation. The *frd* genes (BF638R_4499-4501) were deleted from the *B. fragilis* 638R (TM4000) genome by the following procedure. Regions flanking the deletion were PCR amplified with Phusion polymerase (NEB) and cloned into the BamHI site of pLGB36 (50) using NEBuilder (NEB) and transformed into *Escherichia coli* S17 λ pir. The plasmid was then conjugally transferred from *E. coli* to *B. fragilis*, and cointegrates were selected on BHIS erythromycin plates. The cointegrate was passaged for 5 h in nonselective medium and plated on BHIS plates containing 50 ng/mL anhydrotetracycline (aTC) to select for those that lost the plasmid by double-crossover recombination. Deletion mutants were identified by PCR. For complementation studies, the three *frd* genes were amplified with their native promoter using the primers listed in *SI Appendix*, Table S1 and cloned into the BamHI site of pNBU2. This plasmid was introduced into Δ*frd* by conjugal transfer from *E. coli* S17 λ pir. All plasmids created for this study were sequenced at the Massachusetts General Hospital DNA Core Facility (Boston, MA).

Growth Analyses of *Bacteroides* Species under Anaerobic and Nanaerobic Conditions. All nanaerobic growth in this study was performed at 37 °C in an atmosphere of 1,000 to 1,400 ppm oxygen (0.10 to 0.14%) with a hydrogen concentration between 2.5 and 3.0%, with 10% CO_2 and the remainder nitrogen. The same gas mix was used for the anaerobic conditions without oxygen. Cultures were grown to late log phase in BHIS under either anaerobic or nanaerobic conditions in shaking 5-mL cultures in 100-mL flasks. Aliquots of 3 μL were added to triplicate wells containing 100 μL of BHIS in the outer wells of a 96-well plate and growth was recorded over time at OD_{600} using an Eon high-performance microplate spectrophotometer (BioTek Instruments) with constant shaking between readings. Each of the growth curves summarizes 12 h of growth, with OD_{600} readings taken every 5 min. Each curve of Fig. 1 plots at 1-h intervals the average reading from between two and six replicates of each strain, with a Gompertz growth least-squares fit line connecting them. The logarithmic-scaled graphs in *SI Appendix*, Fig. S1 are an alternate representation of the same data, except the smoothed lines were generated by locally weighted scatterplot smoothing (lowess) regression analysis.

RNA-seq Analysis. Three biological replicate cultures of *Bacteroides fragilis* 638R were grown under anaerobic and nanaerobic conditions (5 mL) in 25-mL vented-top cell culture flasks with shaking for 7 h until an OD_{600} of 0.6 was reached. One milliliter of culture was added to microfuge tubes and sealed in their respective atmospheres, and the bacteria were collected by centrifugation. The supernatant was quickly removed, and the tube was immediately plunged into a dry ice ethanol bath. RNA extraction, library preparation, rRNA depletion, and sequencing (2 × 150 bp; Illumina HiSeq)

were performed by Genewiz. The sequencing reactions of the six samples each produced between 50.9 and 56.1 million reads (15.3 to 16.8 Mb) with mean quality scores of 35.8 to 35.9 for each sample; all samples had ~93% of bases with a quality score of greater than 30. The RNA-seq data returned from Genewiz was evaluated using FastQC (v0.11.9; http://www.bioinformatics.babraham.ac.uk/projects/fastqc/). BBDuk (version 38.76, https://sourceforge.net/projects/bbmap/) was used to remove adapter sequences and to quality trim the raw Illumina reads. Reads with less than 50 bp remaining after QC and adapter trimming were discarded.

The cleaned reads were mapped to the *B. fragilis* 638R genome sequence contained in RefSeq accession no. NC_016776.1 using EDGE-pro (51), chosen because it was developed and optimized for mapping reads to prokaryotic sequences. Per-feature read mapping counts produced by EDGE-pro were evaluated for differential expression using both DESeq2 (52) and edgeR (53). For our analysis, a differentially expressed gene was defined as one that was determined to be expressed on average at least 1.5-fold up or down under nanaerobic conditions relative to anaerobic conditions by both DESeq2 and edgeR, and whose adjusted *P* value (DESeq2) and FDR (edgeR) both were less than or equal to 0.001.

To compile a list of those *B. fragilis* 638R genes that are core genes of the species, a custom blast database comprising all proteins from *B. fragilis* NCTC 9343 (NC_003228.3, GCF_000025985.1), *B. fragilis* YCH46 (NC_006347.1, GCF_000009925.1), *B. fragilis* CL03T12C07 (NZ_JH724181.1, GCF_000273115.1), *B. fragilis* CL05T12C13 (NZ_JH724193.1, GCF_000273135.1), and *B. fragilis* CL07T12C05 (NZ_JH724215.1, GCF_000273155.1) was prepared and searched with blastp (v. 2.9.0+) using the proteome of *B. fragilis* 638R (NC_016776.1, GCF_000210835.1) as the query. Returns were parsed to retain those where the percent similarity and query coverage were both ≥90%. *B. fragilis* 638R query proteins returning at least one qualifying match to each of the five *B. fragilis* genomes were considered to be core genes for this analysis.

A list of essential genes of *B. fragilis* 638R was previously reported (24). We compiled a list of core essential genes as genes included in both the list of core genes and essential genes. Volcano plots were created in Prism, version 8.4.2 (GraphPad Software). BAM files containing the sorted mapping results of EDGE-pro have been deposited to the NCBI SRA database and assigned accession no. PRJNA630209.

Analysis for the Presence of CydAB in the Genomes of Bacteroidales and Diverse Human Gut Symbionts. Two sets of bacteria genomes were retrieved for these analyses. First, a representative set of 173 Bacteroidales genomes was downloaded from NCBI using Entrez queries (Dataset S2). In addition, a 612-genome subset of the Human Gastrointestinal Bacteria Culture Collection (40) that comprises assembled genomes with annotation and protein translations was retrieved from either the GenBank or RefSeq NCBI databases. Profile Hidden Markov models PF01654.17 (Cyt_bd_oxida_I) and PF02322.15 (Cyt_bd_oxida_II) were extracted from the Pfam 32.0 database (54) and compressed into binary form using the hmmpress program from the HMMER, version 3.3, set of utilities (http://hmmer.org/). The proteomes were searched using hmmsearch utilizing the gathering threshold cutoff for each model.

COG Analysis. The *B. fragilis* 638R proteome contained in RefSeq accession no. NC_016776.1 was mapped to COG categories (55) using version 2.0.1 of the stand-alone eggNOG-mapper program (56) and version 5 of the EggNOG database (57) under default settings. Graphs demonstrating the RNA-seq expression levels of these sets of genes were created in GraphPad Prism, version 8.4.2, plotting the least significant fold-change/adjusted *P* value for each as calculated by either DESeq2 or edgeR.

Creation of Red Fluorescent Protein Plasmids. The genes for the red fluorescent proteins, DsRed2, mKate2, and TagRFP, were codon optimized for *Bacteroides* (*SI Appendix*, Fig. S3) and synthesized by Genscript. Each gene was amplified with the primers listed in *SI Appendix*, Table S1 and used to replace the super folder GFP gene and the downstream Flag- and His-tags of plasmid pWW3452 using NEBuilder (Fig. 3*D*). Plasmids were transferred from *E. coli* S17 λ pir to *B. fragilis* 638R by conjugation.

Creation of Linker-*gfp* Vector (pLinkerGFP) for Generation of Fusion Proteins. A 753-bp piece of DNA was synthesized by GenScript containing the superfolder GFP open reading frame (ORF) of pWW3452 (3) including a stop codon without the downstream Flag and His-tags and including the upstream linker region GCAGCTGCAGGAGGTGGA encoding Ala–Ala–Ala–Gly–Gly–Gly used by Basler and Mekalanos (40) for the fusion of proteins to *gfp*. This DNA was amplified with primers linker-GFP-F + R (*SI Appendix*, Table S1). Primers pWW3452 linker GFP_F + R were used to amplify the remainder of pWW3452 lacking the GFP gene. These two parts were amplified using Phusion polymerase (NEB) and joined using NEBuilder (NEB). The plasmid (pLinkerGFP) was sequenced to validate its proper construction. As with the parent pWW3452, the β-lactamase gene is split, which does not affect its ability to confer resistance to ampicillin or carbenicillin. Genes cloned into pLinkerGFP for fusions with GFP at the C terminus should include a single nucleotide upstream of the start codon of the cloned gene to make it out of frame with a portion of an ORF upstream in the regulatory region of pWW3452 (Fig. 3*D*).

Creation of Fusion Proteins with GFP in pLinkerGFP. Three different genes were cloned into pLinkerGFP to place the cloned genes upstream of the linker-GFP. BF638R_1646 (*basp-1*) was amplified from *B. fragilis* 638R, BACOVA_04502 was amplified from *B. ovatus* ATCC 8483, and BF638R_1993 (*tssB*) was amplified from *B. fragilis* 638R using primers listed in *SI Appendix*, Table S1. All genes had an extra nucleotide added before the start codon to place the gene out of frame with a portion of an ORF upstream in the vector. For all clones, the pLinkerGFP vector was amplified with primers pLinkerGFP_F + R. Each gene was joined with the amplified pLinkerGFP using NEBuilder and transformed into *E. coli* S17 λ pir. All plasmids were subject to whole-plasmid sequencing to confirm the correct joining of the segments. Clones were mated from *E. coli* into the appropriate *Bacteroides* strain with subsequent chromosomal integration.

BSAP-1 Overlay Assay. Bacterial cultures tested for BSAP-1 production were dotted onto plates (5 μL) and grown for 12 h. The bacterial growth was removed with a swab and the plates were exposed to chloroform vapor for 15 min. BHIS top agar (4 mL) was inoculated with *B. fragilis* strain 1284 (BSAP-1 sensitive strain) and applied to the plate, and zones of inhibition were imaged after 9 h.

Western Blot Analyses. Antiserum to purified His-BF638R_1994 (TssD) was previously described (26). Supernatants from overnight bacterial cultures were boiled in LDS sample buffer and separated by electrophoresis using NuPAGE 12% polyacrylamide gels (Life Technologies). The contents of the gels were transferred to polyvinylidene difluoride membranes, blocked with skim milk, and probed with (α-TssD) followed by alkaline phosphatase-labeled α-rabbit IgG, and developed with BCIP/NBT (KPL).

T6SS Antagonism Assays. Strains included *B. fragilis* 638R, isogenic mutants ΔT6SS (27), Δ*tssB*, or Δ*tssB*p*tssB-gfp*. Log-phase cultures of these strains were mixed at a ratio of 10:1 (vol/vol) with log-phase *B. vulgatus* CL09T03C04 as the sensitive strain. A volume of 10 μL of the above mixtures was spotted on BHIS plates and incubated overnight in either an anaerobic or nanaerobic atmosphere. The spots were excised and suspended in PBS, and serial 10-fold dilutions were plated to BHIS containing tetracycline (6 μg/mL) to select for *B. vulgatus* CL09T03C04.

Wide-Field Microscopy Analysis of *Bacteroides* Species Grown Anaerobically and Nanaerobically. Bacteria were swabbed from a BHIS erythromycin plate directly into modified M9 medium preincubated overnight in anaerobic or nanaerobic atmosphere with erythromycin and grown shaking at 140 rpm for at least 4 h. Ten microliters of the bacteria were dotted onto 1.5% agarose pads made with modified M9 medium, and a #1.5 coverslip was added and sealed with silicone under nanaerobic or anaerobic conditions. Images were obtained using a Nikon Ti inverted microscope equipped with a Nikon motorized stage, an Andor Zyla 4.2 Plus sCMOS camera, Lumencor SpectraX LED Illumination, Plan Apo lambda 100×/1.45 N.A. Oil Ph3 DM objective lens, and Nikon Elements 4.30 acquisition software. For time-lapse imaging, the microscope was fitted with an Okolab stage top insert incubator. The green channel was imaged using a Chroma 49002 filter cube and a Chroma 49008 filter cube was used for the red channel. Images were adjusted and cropped using Fiji (58). Cell segmentation analyses and quantification of mean single-cell fluorescence signal intensity were carried out using Microbe J (59). The conversion factor from greys to estimated photons was computed using the formula (full well capacity)/((max intensity) − offset) and corresponded to 0.28 estimated photons/intensity level, based on camera settings of 12-bit low gain (full well capacity, 1,100 e-; max intensity, 4,095 intensity levels; camera offset, ~110 gray levels). Fluorescence intensity histograms were computed and plotted in Prism 8.

For time-lapse microscopy of T6SS firing and cellular growth, cells were grown in BHIS broth as described above, to an OD of ~0.5, and 20 μL were spotted onto 1.5% BHIS agarose pads (1 mL, 22 × 22 mm) supplemented with 0.5% (wt/vol) glucose. Pads were transferred to sterile glass-bottom dishes (Greiner Bio-One CELLview), tightly sealed with anaerobic vinyl tape (Coy Laboratory Products), and kept at 37 °C. Cells were imaged at 37 °C as

described above, with 100-ms exposure time in the green channel and 10-s intervals between images. Images were analyzed, and the video was made using Fiji (58). Photobleaching in the green channel was corrected using the Fiji Bleach Correction tool with exponential fit. The Stackreg ImageJ plugin with Rigid Body registration was used to correct for image drift (60). For the video, crops were upscaled using bilinear interpolation.

Data Availability. All study data are included in the article and *SI Appendix*. BAM files containing the sorted mapping results of EDGE-pro have been deposited to the NCBI SRA database and assigned accession no. PRJNA630209 (61).

ACKNOWLEDGMENTS. We thank R. Stephansky and T. Ross-Elliott of the MicRoN Imaging facility at Harvard Medical School for technical assistance, and S. Pryshchep at the Rensselaer Polytechnic Institute Center for Biotechnology and Interdisciplinary Studies Microscopy Core (NSF Grant NSF-MRI-1725984). The Nikon Ti microscope at the MicRoN facility was purchased with the S10 Shared Equipment Grant RR027344-0. M.B. is supported by Swiss National Science Foundation Starting Grant BSSGI0_155778. This work was funded by Public Health Service Grant R01AI132580 (to L.E.C., M.H.M., and B.B.) and R01AI120633 (to L.E.C.) from the NIH/National Institute of Allergy and Infectious Diseases. The funders had no role in study design, data collection and interpretation, or the decision to submit the work for publication.

1. M. Mimee, A. C. Tucker, C. A. Voigt, T. K. Lu, Programming a human commensal bacterium, *Bacteroides thetaiotaomicron*, to sense and respond to stimuli in the murine gut microbiota. *Cell Syst.* **1**, 62–71 (2015).
2. B. Lim, M. Zimmermann, N. A. Barry, A. L. Goodman, Engineered regulatory systems modulate gene expression of human commensals in the gut. *Cell* **169**, 547–558.e15 (2017).
3. W. R. Whitaker, E. S. Shepherd, J. L. Sonnenburg, Tunable expression tools enable single-cell strain distinction in the gut microbiome. *Cell* **169**, 538–546.e12 (2017).
4. L. García-Bayona, L. E. Comstock, Streamlined genetic manipulation of diverse *Bacteroides* and *Parabacteroides* isolates from the human gut microbiota. *MBio* **10**, e01762-19 (2019).
5. S. A. Kuehne, J. I. Rood, D. Lyras, Clostridial genetics: Genetic manipulation of the pathogenic *Clostridia*. *Microbiol. Spectr.* **7** (2019).
6. N. A. Bencivenga-Barry, B. Lim, C. M. Herrera, M. S. Trent, A. L. Goodman, Genetic manipulation of wild human gut *Bacteroides*. *J. Bacteriol.* **202**, e00544-19 (2020).
7. T. Drepper *et al*., Reporter proteins for *in vivo* fluorescence without oxygen. *Nat. Biotechnol.* **25**, 443–445 (2007).
8. L. Teng, K. Wang, J. Xu, C. Xu, Flavin mononucleotide (FMN)-based fluorescent protein (FbFP) as reporter for promoter screening in *Clostridium cellulolyticum*. *J. Microbiol. Methods* **119**, 37–43 (2015).
9. S. O. Seo, T. Lu, Y. S. Jin, H. P. Blaschek, Development of an oxygen-independent flavin mononucleotide-based fluorescent reporter system in *Clostridium beijerinckii* and its potential applications. *J. Biotechnol.* **265**, 119–126 (2018).
10. J. M. Landete *et al*., Anaerobic green fluorescent protein as a marker of *Bifidobacterium* strains. *Int. J. Food Microbiol.* **175**, 6–13 (2014).
11. N. Geva-Zatorsky *et al*., *In vivo* imaging and tracking of host-microbiota interactions via metabolic labeling of gut anaerobic bacteria. *Nat. Med.* **21**, 1091–1100 (2015).
12. H. E. Chia, T. Zuo, N. M. Koropatkin, E. N. G. Marsh, J. S. Biteen, Imaging living obligate anaerobic bacteria with bilin-binding fluorescent proteins. *Curr Res Microbial Sci* **1**, 1–6 (2020).
13. J. L. Mark Welch, Y. Hasegawa, N. P. McNulty, J. I. Gordon, G. G. Borisy, Spatial organization of a model 15-member human gut microbiota established in gnotobiotic mice. *Proc. Natl. Acad. Sci. U.S.A.* **114**, E9105–E9114 (2017).
14. J. L. Mark Welch, B. J. Rossetti, C. W. Rieken, F. E. Dewhirst, G. G. Borisy, Biogeography of a human oral microbiome at the micron scale. *Proc. Natl. Acad. Sci. U.S.A.* **113**, E791–E800 (2016).
15. S. A. Wilbert, J. L Mark Welch, G. G. Borisy, Spatial ecology of the human tongue dorsum microbiome. *Cell Rep.* **30**, 4003–4015.e3 (2020).
16. H. E. Chia, E. N. G. Marsh, J. S. Biteen, Extending fluorescence microscopy into anaerobic environments. *Curr. Opin. Chem. Biol.* **51**, 98–104 (2019).
17. E. Forte, V. B. Borisov, J. B. Vicente, A. Giuffrè, Cytochrome *bd* and gaseous ligands in bacterial physiology. *Adv. Microb. Physiol.* **71**, 171–234 (2017).
18. S. Hill, S. Viollet, A. T. Smith, C. Anthony, Roles for enteric d-type cytochrome oxidase in N_2 fixation and microaerobiosis. *J. Bacteriol.* **172**, 2071–2078 (1990).
19. S. Jünemann, P. J. Butterworth, J. M. Wrigglesworth, A suggested mechanism for the catalytic cycle of cytochrome bd terminal oxidase based on kinetic analysis. *Biochemistry* **34**, 14861–14867 (1995).
20. A. Puustinen, M. Finel, T. Haltia, R. B. Gennis, M. Wikström, Properties of the two terminal oxidases of *Escherichia coli*. *Biochemistry* **30**, 3936–3942 (1991).
21. A. D. Baughn, M. H. Malamy, The strict anaerobe *Bacteroides fragilis* grows in and benefits from nanomolar concentrations of oxygen. *Nature* **427**, 441–444 (2004).
22. J. P. Ouwerkerk *et al*., Adaptation of *Akkermansia muciniphila* to the oxic-anoxic interface of the mucus layer. *Appl. Environ. Microbiol.* **82**, 6983–6993 (2016).
23. C. J. Sund *et al*., The *Bacteroides fragilis* transcriptome response to oxygen and H_2O_2: The role of OxyR and its effect on survival and virulence. *Mol. Microbiol.* **67**, 129–142 (2008).
24. Y. Veeranagouda, F. Husain, E. L. Tenorio, H. M. Wexler, Identification of genes required for the survival of *B. fragilis* using massive parallel sequencing of a saturated transposon mutant library. *BMC Genom.* **15**, 429 (2014).
25. C. Schlieker, H. Zentgraf, P. Dersch, A. Mogk, ClpV, a unique Hsp100/Clp member of pathogenic proteobacteria. *Biol. Chem.* **386**, 1115–1127 (2005).
26. P. I. Hanson, S. W. Whiteheart, AAA+ proteins: Have engine, will work. *Nat. Rev. Mol. Cell Biol.* **6**, 519–529 (2005).
27. M. Chatzidaki-Livanis, N. Geva-Zatorsky, L. E. Comstock, *Bacteroides fragilis* type VI secretion systems use novel effector and immunity proteins to antagonize human gut Bacteroidales species. *Proc. Natl. Acad. Sci. U.S.A.* **113**, 3627–3632 (2016).
28. M. J. Coyne, L. E. Comstock, Type VI secretion systems and the gut microbiota. *Microbiol. Spectr.* **7** (2019).
29. R. L. Morris, T. M. Schmidt, Shallow breathing: Bacterial life at low O_2. *Nat. Rev. Microbiol.* **11**, 205–212 (2013).
30. J. D. Pédelacq, S. Cabantous, T. Tran, T. C. Terwilliger, G. S. Waldo, Engineering and characterization of a superfolder green fluorescent protein. *Nat. Biotechnol.* **24**, 79–88 (2006).
31. N. M. Koropatkin, E. C. Martens, J. I. Gordon, T. J. Smith, Starch catabolism by a prominent human gut symbiont is directed by the recognition of amylose helices. *Structure* **16**, 1105–1115 (2008).
32. E. D. Sonnenburg *et al*., Specificity of polysaccharide use in intestinal *Bacteroides* species determines diet-induced microbiota alterations. *Cell* **141**, 1241–1252 (2010).
33. S. Rakoff-Nahoum, M. J. Coyne, L. E. Comstock, An ecological network of polysaccharide utilization among human intestinal symbionts. *Curr. Biol.* **24**, 40–49 (2014).
34. S. Rakoff-Nahoum, K. R. Foster, L. E. Comstock, The evolution of cooperation within the gut microbiota. *Nature* **533**, 255–259 (2016).
35. M. Chatzidaki-Livanis, M. J. Coyne, L. E. Comstock, An antimicrobial protein of the gut symbiont *Bacteroides fragilis* with a MACPF domain of host immune proteins. *Mol. Microbiol.* **94**, 1361–1374 (2014).
36. M. Basler, Type VI secretion system: Secretion by a contractile nanomachine. *Philos. Trans. R. Soc. London. Ser. B Biol. Sci.* **370**, 20150021 (2015).
37. M. J. Coyne, K. G. Roelofs, L. E. Comstock, Type VI secretion systems of human gut Bacteroidales segregate into three genetic architectures, two of which are contained on mobile genetic elements. *BMC Genom.* **17**, 58 (2016).
38. A. G. Wexler *et al*., Human symbionts inject and neutralize antibacterial toxins to persist in the gut. *Proc. Natl. Acad. Sci. U.S.A.* **113**, 3639–3644 (2016).
39. A. L. Hecht *et al*., Strain competition restricts colonization of an enteric pathogen and prevents colitis. *EMBO Rep.* **17**, 1281–1291 (2016).
40. M. Basler, J. J. Mekalanos, Type 6 secretion dynamics within and between bacterial cells. *Science* **337**, 815 (2012).
41. S. C. Forster *et al*., A human gut bacterial genome and culture collection for improved metagenomic analyses. *Nat. Biotechnol.* **37**, 186–192 (2019).
42. H. J. Haiser *et al*., Predicting and manipulating cardiac drug inactivation by the human gut bacterium *Eggerthella lenta*. *Science* **341**, 295–298 (2013).
43. A. Mukhopadhyay *et al*., Cell-wide responses to low-oxygen exposure in *Desulfovibrio vulgaris* Hildenborough. *J. Bacteriol.* **189**, 5996–6010 (2007).
44. L. Albenberg *et al*., Correlation between intraluminal oxygen gradient and radial partitioning of intestinal microbiota. *Gastroenterology* **147**, 1055–1063.e8 (2014).
45. Y. Shen *et al*., Outer membrane vesicles of a human commensal mediate immune regulation and disease protection. *Cell Host Microbe* **12**, 509–520 (2012).
46. W. Elhenawy, M. O. Debelyy, M. F. Feldman, Preferential packing of acidic glycosidases and proteases into *Bacteroides* outer membrane vesicles. *MBio* **5**, e00909-14 (2014).
47. C. A. Hickey *et al*., Colitogenic *Bacteroides thetaiotaomicron* antigens access host immune cells in a sulfatase-dependent manner via outer membrane vesicles. *Cell Host Microbe* **17**, 672–680 (2015).
48. J. K. Maerz *et al*., Outer membrane vesicles blebbing contributes to *B. vulgatus* mpk-mediated immune response silencing. *Gut Microb.* **9**, 1–12 (2018).
49. W. A. Bryant *et al*., *In silico* analysis of the small molecule content of outer membrane vesicles produced by *Bacteroides thetaiotaomicron* indicates an extensive metabolic link between microbe and host. *Front. Microbiol.* **8**, 2440 (2017).
50. T. Ito *et al*., Genetic and biochemical analysis of anaerobic respiration in *Bacteroides fragilis* and its importance *in vivo*. *MBio* **11**, e03238-19 (2020).
51. T. Magoc, D. Wood, S. L. Salzberg, EDGE-pro: Estimated degree of gene expression in prokaryotic genomes. *Evol. Bioinform. Online* **9**, 127–136 (2013).
52. M. I. Love, W. Huber, S. Anders, Moderated estimation of fold change and dispersion for RNA-seq data with DESeq2. *Genome Biol.* **15**, 550 (2014).
53. M. D. Robinson, D. J. McCarthy, G. K. Smyth, edgeR: A Bioconductor package for differential expression analysis of digital gene expression data. *Bioinformatics* **26**, 139–140 (2010).
54. S. El-Gebali *et al*., The Pfam protein families database in 2019. *Nucleic Acids Res.* **47**, D427–D432 (2019).
55. R. L. Tatusov *et al*., The COG database: An updated version includes eukaryotes. *BMC Bioinf.* **4**, 41 (2003).
56. J. Huerta-Cepas *et al*., Fast genome-wide functional annotation through orthology assignment by eggNOG-mapper. *Mol. Biol. Evol.* **34**, 2115–2122 (2017).
57. J. Huerta-Cepas *et al*., eggNOG 5.0: A hierarchical, functionally and phylogenetically annotated orthology resource based on 5090 organisms and 2502 viruses. *Nucleic Acids Res.* **47**, D309–D314 (2019).
58. J. Schindelin *et al*., Fiji: An open-source platform for biological-image analysis. *Nat. Methods* **9**, 676–682 (2012).
59. A. Ducret, E. M. Quardokus, Y. V. Brun, MicrobeJ, a tool for high throughput bacterial cell detection and quantitative analysis. *Nat. Microbiol.* **1**, 16077 (2016).
60. P. Thévenaz, U. E. Ruttimann, M. Unser, A pyramid approach to subpixel registration based on intensity. *IEEE Trans. Image Process.* **7**, 27–41 (1998).
61. M. J. Coyne, L. E. Comstock, RNASeq mapping of Bacteroides fragilis 638R grown under aerobic and nanaerobic conditions. NCBI SRA database. https://www.ncbi.nlm.nih.gov/bioproject?term=PRJNA630209. Deposited 4 May 2020.